

Chromium agglomeration induced by Fe⁺ ion irradiation of Fe-10at%Cr

S. Pantousa^{a,b}, A.J. London^c, K. Mergia^{a,*}, A. Ionescu^d, E. Manios^a, P. Tsavalas^a, S. Dellis^a, C. Kinane^e, S. Langridge^e, A. Caruana^e, U. Kentsch^f, S. Messoloras^a

^a Institute of Nuclear and Radiological Sciences and Technology, Energy and Safety, NCSR "Demokritos", Athens 15341, Greece

^b Department of Physics, National and Kapodistrian University of Athens, Athens 15784, Greece

^c UK Atomic Energy Authority, Culham Science Centre, Oxfordshire OX14 3DB, United Kingdom

^d Cavendish Laboratory, University of Cambridge, J J Thomson Avenue 19, Cambridge CB3 0HE, United Kingdom

^e ISIS Neutron and Muon Source, Rutherford Appleton Laboratory, Harwell Science and Innovation Campus, Chilton OX11 0QX, United Kingdom

^f Ion Beam Center, Helmholtz-Zentrum Dresden-Rossendorf, Germany

ARTICLE INFO

Keywords:

Fe-Cr alloys

Ion irradiation

Cr depletion

Polarized neutron reflectivity

Atom probe tomography

ABSTRACT

Fe-Cr alloys serve as model alloys for the investigation of radiation induced effects in ferritic-martensitic steels which are candidate structural materials for future fusion reactors. In this work the effect of Cr segregation and/or agglomeration in 490 keV Fe⁺ ion irradiated Fe-10at%Cr alloys in the form of thin films is investigated. The irradiations took place at 300 °C at doses ranging from 0.5 to 20 displacements per atom (dpa). Polarized Neutron Reflectivity (PNR) measurements were used for the determination of the solute Cr concentration in the Fe-Cr matrix. Cr depletion from the Fe-Cr matrix up to 2.4 at% was found. This is related to solute Cr decrement as the accumulated dose increases. After the damage of 4 dpa, solute Cr reaches the asymptotic value of 8.4 at%, close to that of the thermodynamic equilibrium in Fe-Cr. Atom Probe Tomography (APT) measurements showed that after irradiation Cr accumulates into clusters the majority of which is co-located with oxygen.

1. Introduction

Ferritic – martensitic steels are the preferred choice for structural materials in fusion power plants, because of their advantageous properties including low activation, good mechanical and thermomechanical properties, chemical compatibility with the other reactor components they interface with, and radiation resistance [1–5]. Therefore, the study of radiation-induced effects on these materials in the temperature operating window for their use is of paramount technological and scientific significance. The temperature of 300 °C lies within the operating temperature range for the blanket concept candidates for DEMO. Specifically, in the case of the Water – Cooled Lithium – Lead (WCLL) breeding blanket concept, the structural materials will be cooled to 295–328 °C, and will be exposed to temperatures that is planned to not exceed 550 °C [6], while for the Helium – Cooled Peddle Bed (LCPB) concept the operating temperature will be in the range from 300 °C to 500 °C [7,8].

Fe-Cr alloys serve as model systems for the investigation of ferritic – martensitic steels' behavior within the fusion environment, in which they have to endure both radiation damage and thermal aging. The

presence of Cr plays a crucial role in the behaviour of these alloys under irradiation [9]. It has been shown that alloys containing approximately 10 at% Cr demonstrate the most favorable characteristics for such applications. They present good swelling resistance under irradiation, minimum radiation induced ductile to brittle transition temperature (DBTT) shift and corrosion resistance [10–13]. At the same time they are prone to embrittlement due to α - α' decomposition at temperatures below 400 °C according to Bonny et al. [14] and below 370 °C according to Zhao et al. [15] and Xiong et al. [16].

The deuterium–tritium (D-T) fusion reaction, the most energetically efficient reaction for power production, has the greatest cross-section at the lowest temperature, releasing the highest amount of energy [17]. High-energy neutrons, having a kinetic energy of 14.1 MeV, is the by-product of these reactions and when impinging on Fe-Cr alloys they generate primary knock-on Fe and Cr atoms (PKAs) with a mean energy of 490 keV. Therefore, the damage caused by energetic neutrons that are present in a fusion environment can be imitated by self-ion irradiations with this energy, as reported in previous experimental work [18–21]. Ion irradiations offer numerous benefits, including precision in the definition of ion energies and fluxes, controlled irradiation temperature,

* Corresponding author.

E-mail address: kmergia@ipta.demokritos.gr (K. Mergia).

<https://doi.org/10.1016/j.nme.2024.101680>

Received 11 December 2023; Received in revised form 3 May 2024; Accepted 20 May 2024

Available online 22 May 2024

2352-1791/© 2024 The Authors. Published by Elsevier Ltd. This is an open access article under the CC BY-NC-ND license (<http://creativecommons.org/licenses/by-nc-nd/4.0/>).

short irradiation times and cost-effectiveness [22,23]. Additionally, the ability to perform experiments under well-controlled irradiation conditions in a systematic manner, without the complexities associated with neutron irradiation, providing a test bed for validating modeling of the radiation damage of materials. On the other hand, the penetration depth of ions depends on the ion energy and there is a spatial distribution of damage, reaching a peak level on the order of micrometer in depth.

Aim of this work, in conjunction with our previous work [18,19], is to study the effects of Fe^+ ion irradiation on Fe-10at%Cr alloys at 300 °C, for contributing to the development of theoretical models of radiation damage under fusion reactor conditions. In order to achieve the specified purpose well defined sample state and radiation conditions are required such as to be easily implemented in models and the results of calculations to be directly compared with experimental data. These premises impose the following experimental requirements: a) Fe^+ ion energy to be relevant to the mean energy of PKAs of 14 MeV neutrons, b) Fe^+ ion total deposited energy almost constant within the depth of the sample, c) minimum implantation effects, and d) well defined sample surface boundaries. These prerequisites are met by irradiating with 490 keV Fe^+ ions 70 nm thick Fe-10at%Cr films sandwiched within SiO_2 and Cr_2O_3 (for details see [19]).

2. Materials and experimental methods

2.1. Irradiation simulations

Taking into consideration the limited penetration depth of heavy ions, the most appropriate sample form for investigating the irradiation-induced effects of Fe^+ ions is that of a film. The optimal film thickness can be determined by taking into consideration the damage profile and the implantation probability of the ions as a function of depth in the material. For this reason, simulation of 490 keV Fe^+ ions impinging on a Fe-10at%Cr target was performed employing the SRIM-2013 software [24,25]. As described in [19] the “Detailed calculation with Full Damage cascades” option was used, while for both Fe and Cr atoms the displacement energy was set to 40 eV [26,27] and the lattice and surface binding energy set to zero (0 eV). The irradiation doses in displacements per atom (dpa) are presented in Table 1 and they were calculated from the total number of recoiled Fe and Cr atoms tabulated in the *Range.txt* file. It must be noted that the dpa calculated employing this approach is 49 % higher than the NRT dpa that results from that recommended by Agarwal et al. [28] and Sun et al. [29] SRIM Full Cascades energy method using the phonon energy from the *Phonon.txt* file and 47 % higher than the NRT dpa that results from the “Quick” Kinchin and Pease option recommended by Stoller [30].

The total recoiled Fe and Cr atoms per incident ion and per nm unit of depth are presented in Fig. 1, as a function of depth. In the same plot the implantation probability per incident Fe^+ ion and the integrated implanted ions for the maximum irradiation dose are also illustrated as a function of depth.

Table 1
Irradiation conditions of Fe-10at%Cr films.

Irr. Temperature (°C)	Energy (keV)	Flux (ions•cm ⁻² •s ⁻¹)	Fluence (ions•cm ⁻²)	Irr. Time (min)	Dose (dpa)
300	490	1×10^{12}	2.3×10^{14}	4	0.5
			4.6×10^{14}	8	1
			9.2×10^{14}	16	2
			1.8×10^{15}	32	4
			2.8×10^{15}	49	6
			3.7×10^{15}	65	8
			5.5×10^{15}	97	12
			7.4×10^{15}	131	16
			9.2×10^{15}	163	20

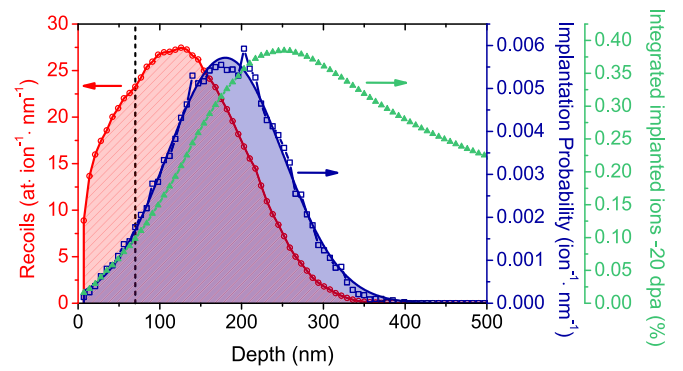


Fig. 1. Recoils (red open circles), implantation probability (blue open squares) and integrated implanted ions for the highest accumulated dose (green solid triangles) as a function of depth that resulted from SRIM calculations for 490 keV Fe^+ ions on Fe-10at%Cr. The vertical dashed line at 70 nm indicates the thickness of the films used in this study. The solid blue line for the implantation probability is a Gaussian fit.

2.2. Sample fabrication and irradiations

As elucidated in reference [19] and is reflected in Fig. 1 the film thickness of 70 nm fulfills the requirement to reduce the implantation of ions in the alloy while also ensuring that produced recoils are sufficient for the radiation induced phenomena to take place. Thus, Fe-10at%Cr alloys in the form of thin films having thickness of 70 nm were fabricated on 10×10 mm Si/SiO₂(300 nm) substrates. A thin passivation layer of Cr, approximately 4 nm thick, was deposited on top of the Fe-Cr films to prevent their oxidization. The fabrication was performed using DC magnetron sputtering at the Materials Growth Facility (MGF) located in the Cavendish Laboratory of the University of Cambridge. The details regarding the fabrication process can be found in [19].

Energy dispersive X-ray analysis of the Fe-10at%Cr sputtering target at the energy of 30 keV showed no oxygen with a detection limit of 0.1 at %. During the deposition no purplish color in the plasma was observed that would indicate oxygen contamination in the chamber, or in the sputtering Argon gas, or on the target surface.

Both the O and Cr atoms that through recoil from the top chromium oxide layer are implanted into the Fe-Cr layer reach a mean depth of 0.5 nm, i.e. the implantation profile is almost the same for both species. These calculations imply that during irradiation the protective chromium layer becomes thicker. As both Cr and O are ejected in the 0.5 nm layer is unlikely that the Cr-O bond is broken and consequently O diffuses to the bulk of the material.

2.3. Fe^+ ion irradiation

The ion irradiation was carried out at the 500 kV air insulated accelerator made by HVEE of the Ion Beam Center in HZDR in Dresden, Germany. The irradiation conditions are presented in Table 1. The FeCr films were placed under high vacuum ($10^{-7} - 10^{-6}$ mbar) and were irradiated with 490 keV Fe^+ ions at 300 °C up to 20 dpa with a damage rate of 0.002 dpa/s. During the irradiation the temperature was controlled through a K-type thermocouple attached on the sample holder and was monitored with a calibrated infrared camera. The ion beam was incident at 7° with respect to the sample normal and the sample's surface was raster scanned in the horizontal and vertical direction with a frequency of 1 kHz.

2.4. Polarized neutron reflectivity measurements

Polarized Neutron Reflectivity (PNR) technique as outlined by J. F. Anker [31] can be used for the determination of the magnetization of thin films as a function of depth with nanometric resolution. The PNR

measurements of the Fe-10at%Cr samples were carried out at the POLREF facility [32,33], at the ISIS neutron spallation source, at the Rutherford-Appleton Laboratory (RAL) in United Kingdom and the experimental details regarding these measurements are presented in [19]. The analysis of the PNR data was performed employing the GenX software [34,35].

2.5. Atom probe tomography measurements

The microstructure of the samples was investigated employing Atom Probe Tomography (APT) technique. Samples were fabricated at the Materials Research Facility (MRF) of the UK Atomic Energy Authority (UKAEA). Sharp needle shaped samples were made using the Focused Ion Beam (FIB) liftout technique as detailed elsewhere [36]. The whole layer of the film was lifted out “top-down”, placed on a temporary support and then rotated 90°, as shown in Fig. 2. Then this bar of material is lifted and cut into micron-chunks on an array of silicon posts for sharpening. This method allows the analysis in the plane of the thin film, parallel to the original surface. The final tip from the FIB contained most or all of the Fe-Cr layer. 30 kV Ga ions were employed for the main milling, while the final cleaning step was performed with a 2 kV Ga beam to limit Ga-damage/implantation. APT allows for the three-dimensional reconstruction and analysis of the atomic arrangement within a material with sub-nm resolution [37,38]. APT measurements of two Fe-10at%Cr films (one non-irradiated and one irradiated with the dose of 16 dpa) were performed at the Nuclear Materials Atom Probe (NuMAP) Facility at the University of Oxford. A LEAP 5000XR was used with a 50 pJ laser pulse with 200 kHz repetition rate. The specimen based temperature was held at 50 K. At least two successful volumes were reconstructed from each condition, non-irradiated and irradiated. The total ion counts were 9.8, 15.2, 2.5 and 7.5 million ions for the two non-irradiated and two irradiated volumes, respectively. The data was reconstructed using IVAS 3.8.4 with a $k = 3.3$ and ICF of 1.45. Clusters were defined employing the maximum separation method [39], using two different settings, one to isolate the O-rich clusters and one to remove any oxygen to leave the matrix behind, {Knn 4, d_{\max} 1.0 nm, N_{\min} 100, L 0.5 nm, with core-ions Fe₂O, FeO} and {Knn 1, d_{\max} 2.0 nm, N_{\min} 10, L 0.5 nm, core-ions Fe₂O, FeO} respectively. For the matrix measurement, these are the ions which are not clustered using the second set of settings stated above. Note that the clustering selection used to leave the matrix behind was much more sensitive, with a lower Knn, larger d_{\max} and smaller N_{\min} to avoid the periphery of clusters. This approach was applied as oxygen tends to migrate laterally on the sample surface during evaporation. All compositions were local-background subtracted and peak-overlap solved [40].

3. Results

3.1. Polarized neutron reflectivity results

The magnetization of the Fe-Cr films as a function of irradiation dose was quantified using PNR measurements and is presented in Fig. 3. The methodology of the determination of the magnetization and of the solute Cr concentration is detailed in our previous work [18,19].

The magnetization increases as the dose increases up to about the dose of 4 dpa and remains almost constant, having an average value of $(1.915 \pm 0.002) \mu_B/\text{at}$ for further increase of the dose. This behavior is described by the relationship

$$m(d) = m_0 + m_{\text{incr}}(1 - e^{-d/d_m}) \quad (1)$$

where m_0 is the initial magnetization, m_{incr} is the increase of magnetization after irradiation, $m_{\text{eq}} = m_{\text{incr}} + m_0$ is the magnetization equilibrium value attained at large doses and d_m the radiation damage saturation constant for magnetization and is depicted by the black solid line in Fig. 3. The least squared fitted values of these parameters are presented in Table 2.

The solute Cr concentration, C_{Cr} , in the Fe-Cr matrix of the films was determined from their measured magnetization using the relationship [18]

$$C_{\text{Cr}}(\text{at}\%) = A \left(\frac{\text{at}\%}{\mu_B/\text{at}} \right) (m_0 - m) \quad (2)$$

where $A = (41.0 \pm 1.4) \text{ at}\%/\mu_B/\text{at}$ and $m_0 = (2.12 \pm 0.01) \mu_B/\text{at}$ are experimentally determined constants. Eq. (2) results from empirical fitting of magnetization data originating from measurements both on FeCr bulk alloys and FeCr films with known C_{Cr} up to 15 at% employing PNR and Vibrating Sample Magnetometer techniques [18]. In Fig. 3 the variation of C_{Cr} is presented as a function of irradiation dose. The solid line is the least squares fitting of the data using the equation

$$C(d) = C_0 - C_{\infty}(1 - e^{-d/d_c}) \quad (3)$$

where C_0 is the initial Cr content, C_{∞} is the decrease in Cr concentration, $C_{\text{eq}} = C_0 - C_{\infty}$ is the equilibrium concentration and d_c the radiation damage saturation constant for the Cr concentration. The values of C_0 , C_{∞} , C_{eq} and d_c are presented in Table 2.

The PNR measurements also show the oxidation of the Cr cover layer to Cr₂O₃ at all irradiation doses. It should be also noted that the scattering length of Cr and Fe are very different for neutrons contrary to the corresponding scattering factors for X-rays which are very close. Thus, neutron reflectivity is sensitive to Cr structures.

The analysis of the PNR spectra does not show any depth dependence of the magnetization, indicating that Cr depletion is homogeneous

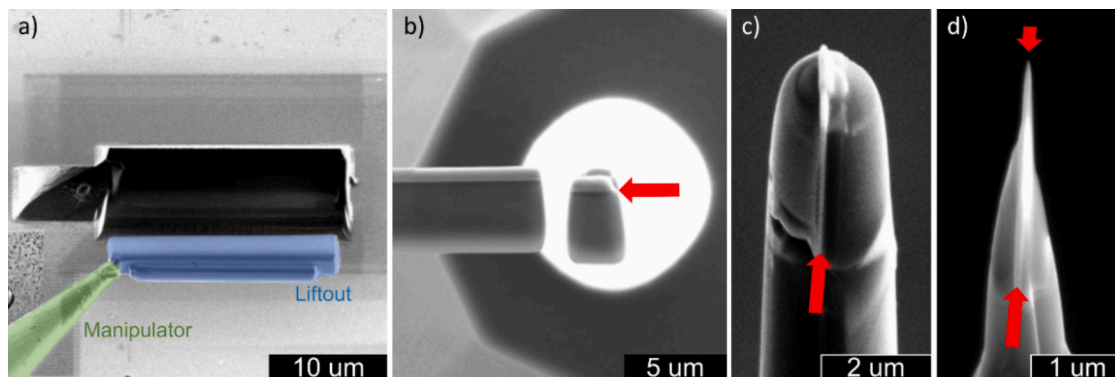


Fig. 2. Focused Ion Beam preparation of atom probe samples. a) Shows the initial liftout, with protective Pt-layer, which is rotated 90° along the axis of the beam *ex situ*. b) Cut sample mounted on a silicon post, film location is indicated by a red arrow, looking top down in the plane of the original film. c) Partial sharpening shown side on. d) Final sharpening with the thin Fe-Cr layer indicated by the red arrows.

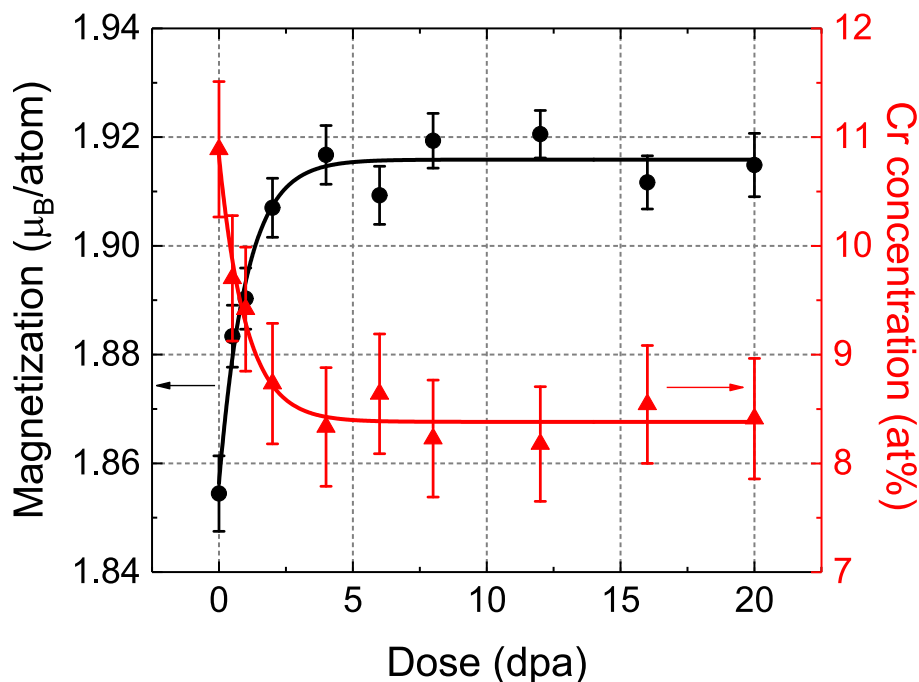


Fig. 3. Magnetization and solute Cr concentration in the Fe-Cr matrix as a function of irradiation dose for the Fe-10at%Cr(70 nm) films irradiated at 300 °C [19] and at the dose rate of 0.002 dpa/s. The solid lines are the least squares fittings of Eqs. (1) and (3) to the experimental data.

Table 2

Least square fitted values for the parameters in Eqs. (1) and (3) to the experimental data in Fig. 3.

m_0 (μ_B/at)	m_{incr} (μ_B/at)	m_{eq} (μ_B/at)	d_m (dpa)	C_0 (at%)	C_∞ (at%)	C_{eq} (at%)	d_c (dpa)
1.856 ± 0.005	0.060 ± 0.006	1.92 ± 0.01	1.0 ± 0.2	10.8 ± 0.2	2.4 ± 0.2	8.4 ± 0.3	1.0 ± 0.2

through the film thickness.

3.2. Atom probe tomography results

APT measurements were performed to both the non-irradiated sample and the sample that was irradiated with the dose of 16 dpa at 300 °C. In Fig. 4 and Fig. 5 the two-dimensional distribution of the Cr and O atoms in the film plane are presented for the non-irradiated and the irradiated sample, respectively. In Fig. 6 and Fig. 7 cross sectional images of the two dimensional Cr and O distributions of the non-irradiated and irradiated samples are depicted. It is observed that before the irradiation Cr is distributed homogeneously in the Fe-Cr matrix, while after the irradiation Cr accumulates into clusters, co-located with oxygen impurities. In the non-irradiated sample the Cr distribution is homogeneous as observed in Fig. 4a and Fig. 6a. The phase separation after irradiation does not show any non-uniformity along the thickness direction (Fig. 7). This is in agreement with the analysis of the PNR spectra that does not show any depth dependent effects of the magnetization which would indicate depth dependent Cr content as discussed in the previous section. The size of the Cr clusters is in the range from about 1 to 8 nm, while the Cr concentration in these clusters does not exceed 50 at% (Fig. 5a).

The non-irradiated sample presents some oxygen clusters (Fig. 4b and Fig. 6b) for which the origin of oxygen will be discussed below and in the next section.

The Cr-rich clusters in the irradiated sample were measured to have increased concentrations of O and Cr in them. This is further supported by proximity-histogram analysis (Fig. 8) showing the Cr and O

concentration around the interface (zero distance) from iso-concentration surfaces of 12 at% Cr concentration.

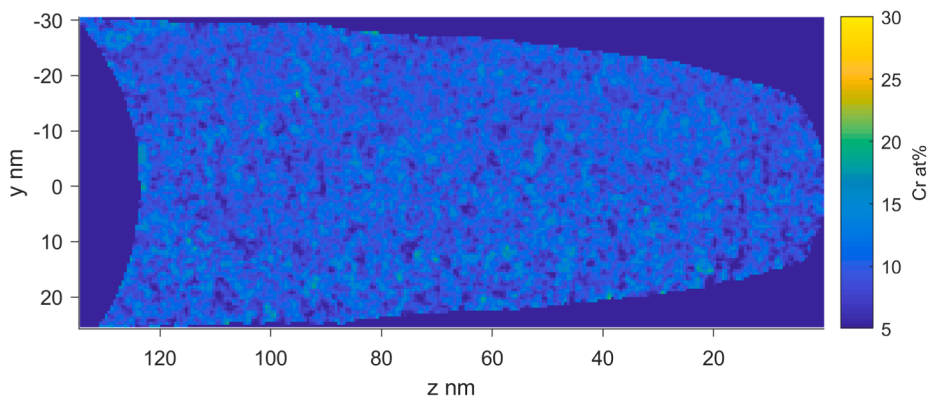
The Cr, Fe and O content (mean values together with the standard deviation at 95 % confidence level) in the total of the Fe-10at%Cr film, in the matrix, in the O-rich clusters for the non-irradiated sample and in the Cr-rich clusters for the irradiated at 16 dpa sample are presented in Table 3. <1 at% levels of H, C, N, Si, Mn and Ga were also detected.

The total Cr content in the non-irradiated and irradiated sample is found (9.99 ± 0.04) at% and (9.7 ± 1.7) at% (Table 3), respectively, in good agreement with the values resulted from X-ray fluorescence (XRF) spectroscopy ((9.5 ± 1.0) at%) and Rutherford backscattering spectroscopy (RBS) measurements using 17.5 MeV oxygen ions ((11 ± 1) at%).

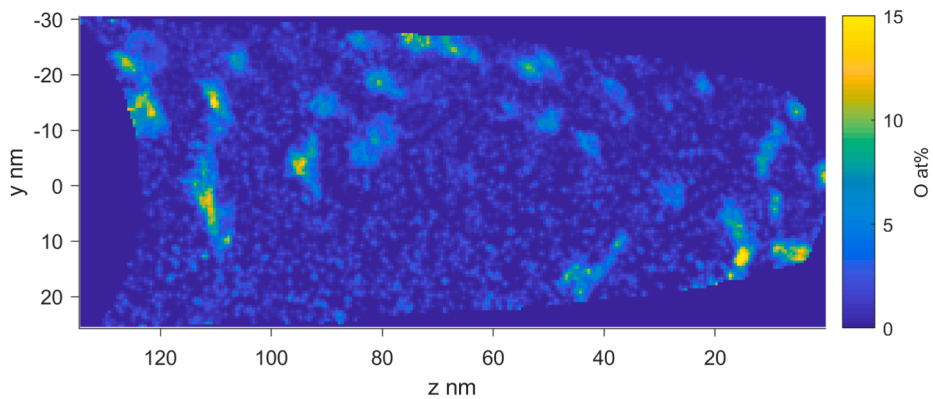
The oxygen in the matrix in the non-irradiated sample in one APT tip is 0.20 at% whereas on the other tip is 0.09 at%. Difference between the tips occurs also in the irradiated sample, one tip has matrix oxygen concentration 1.16 at% whereas the other tip has 0.15 at%. These indicate the existence of a very inhomogeneous distribution of oxygen in the sample. In addition the matrix oxygen concentration in the irradiated sample is much higher than that of the non-irradiated one. As discussed in section 2.2, it has been excluded the implantation of oxygen from the chromium oxide layer during ion irradiation. Taking into account the large variations of the oxygen content in the matrix between two tips, indicating inhomogeneous oxygen distribution, the total oxygen concentration in Table 3 is not representative of the samples and the difference in oxygen content between irradiated and non-irradiated is questionable (the large errors also support this conclusion).

In the non-irradiated sample the oxygen is mainly appearing in O-rich clusters of (6.4 ± 0.2) at% O content. The Cr content within these clusters of around (9.0 ± 0.2) at% is very close to that of the matrix indicating that there is no Cr clustering (Table 3). The O-rich clusters in the non-irradiated sample have sizes in the range from 1 to 10 nm in the film plane (Fig. 4b) and they are elongated in the direction normal to the sample surface as it can be seen in Fig. 6b.

The O-rich clusters of the non-irradiated sample have a radius of gyration of (6.8 ± 3.8) nm (the error denotes one standard deviation and a sampling number of 62), and a number density of $1 \times 10^{23} m^{-3}$. The

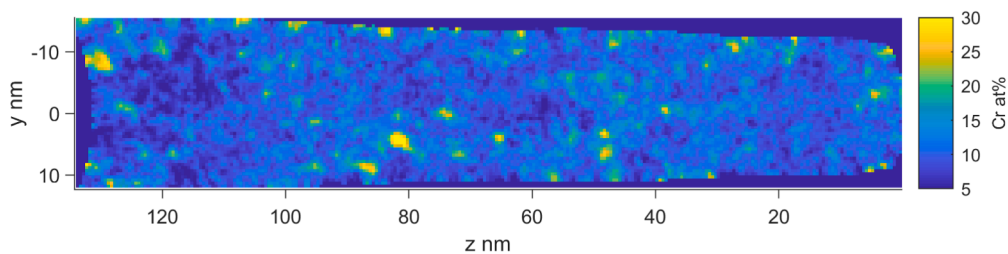


(a)

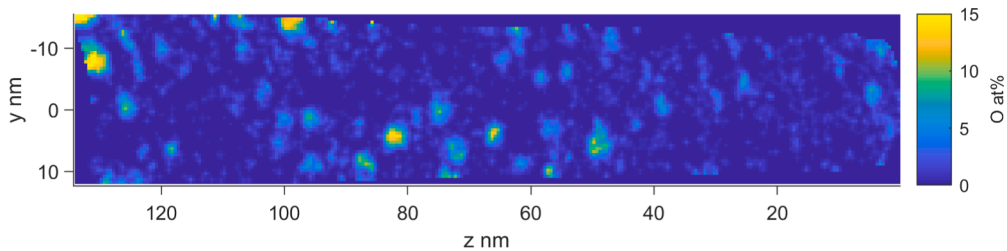


(b)

Fig. 4. 2D distribution of (a) Cr and (b) O atoms in the non – irradiated Fe-10at%Cr film, 5 nm depth from the middle of the Fe-Cr layer into the page of 3D data, looking normal to the film surface. The concentration axis refers to the atomic concentration.



(a)



(b)

Fig. 5. 2D distribution of (a) Cr and (b) O atoms in the Fe-10at%Cr film after 490 keV Fe⁺ ion irradiation at 300 °C at the dose of 16 dpa, 5 nm depth from the middle of the Fe-Cr layer into the page of 3D data, looking normal to the film surface. The concentration axis refers to the atomic concentration.

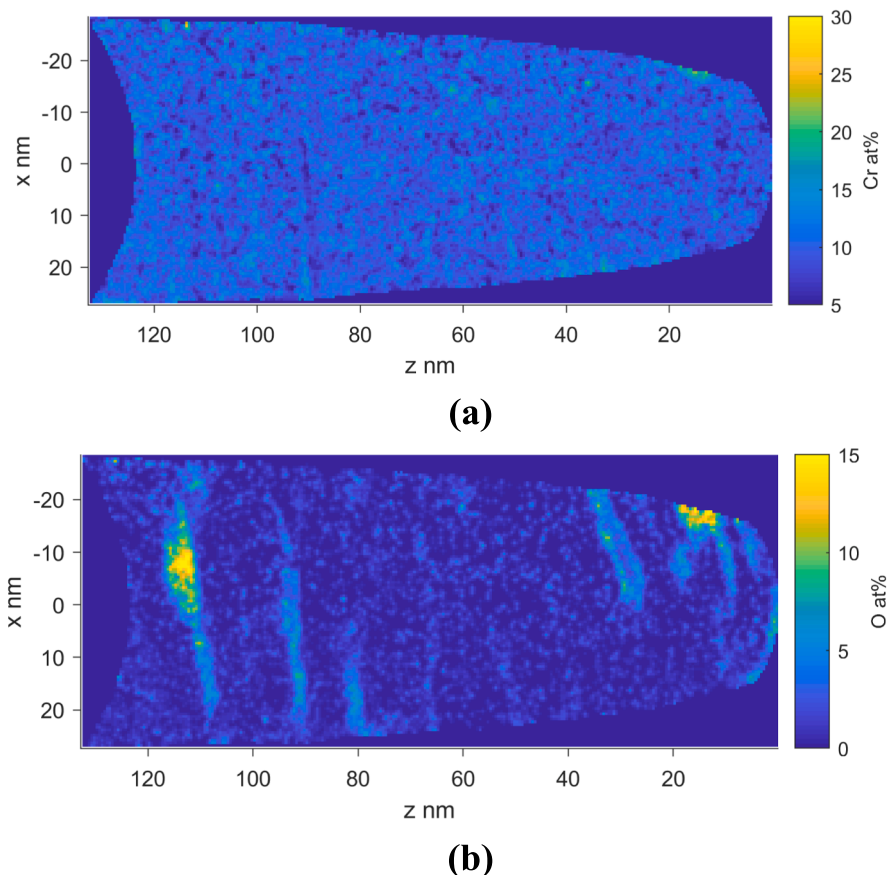


Fig. 6. Cross sectional 2D distribution of (a) Cr and (b) O atoms in the non-irradiated Fe-10at%Cr film. y axis is perpendicular to the sample surface.

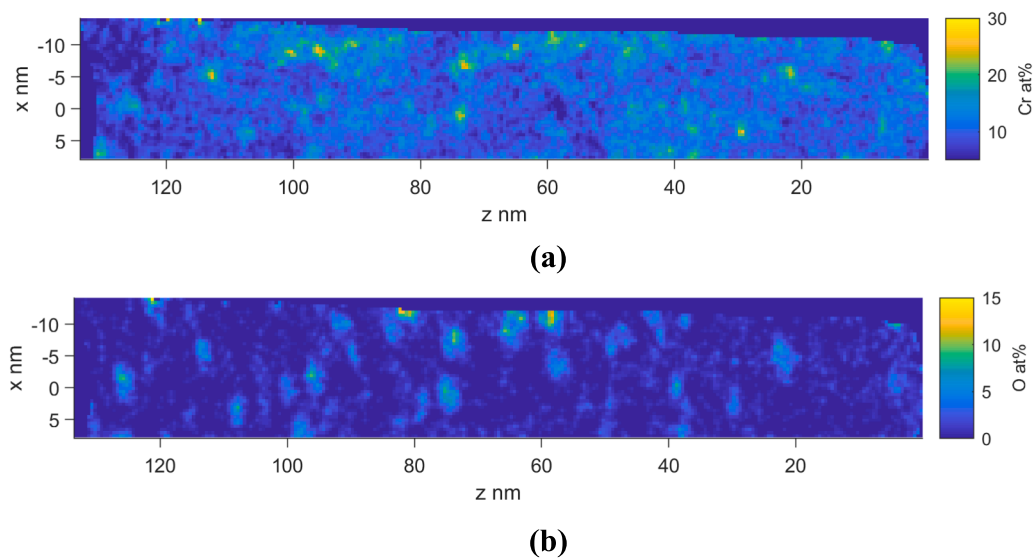


Fig. 7. Cross sectional 2D distribution of (a) Cr and (b) O atoms in the Fe-10at.%Cr film after 490 keV Fe^+ ion irradiation at 300 °C at the dose of 16 dpa. y axis is perpendicular to the sample surface.

Cr-rich clusters in the irradiated sample present a radius of gyration of (2.4 ± 1.4) nm (the error denotes one standard deviation, and a sampling number of 138) and their number density is found $6 \times 10^{23} \text{ m}^{-3}$.

In [Table 3](#) the solute Cr concentration in the matrix of the Fe-Cr film is presented for the two samples. These values are in agreement with the solute Cr concentration deduced from PNR measurements, which are

(10.8 ± 0.2) at% in the case of the non-irradiated sample and (8.5 ± 0.5) at% in the case of the irradiated sample for the dose of 16 dpa ([Fig. 3](#)).

The Cr and O concentration around the interfaces of the clusters derived from *iso*-concentration surfaces of 12 at% Cr is presented in the proximity histograms of [Fig. 8](#). Very similar diagrams (not shown) are derived if *iso*-concentration surfaces of 2 at% O are utilized. From [Fig. 8](#)

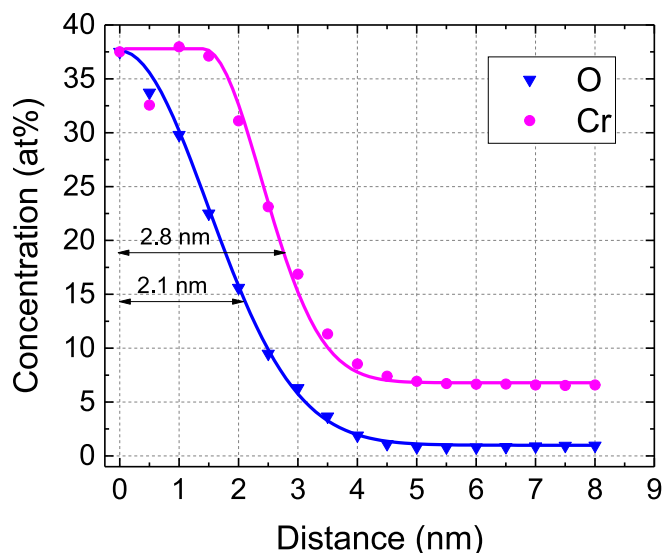


Fig. 8. Proximity histograms showing the Cr and O concentration around the interface from iso-concentration surfaces of 12 at% Cr concentration. The x axis has been shifted by 4.15 nm with respect to the zero corresponding to the interface. Points: experimental data. Indicative continuous lines correspond to equations

$$C_{Cr}(\text{at}\%) = 37.8 \text{ for } x \leq 1.4 \text{ nm}, C_{Cr}(\text{at}\%) = 6.8 + 31 \cdot \exp\left(-\left(\frac{x-1.4}{1.4}\right)^2\right) \text{ for } x >$$

1.4 nm and $C_O(\text{at}\%) = 1.0 + 36.6 \cdot \exp\left(-\left(x \cdot 2.1\right)^2\right)$ for the Cr and O, respectively.

Table 3

Composition of Cr, Fe and O in at% in the total of the Fe-10at%Cr film, in the clusters and in the matrix for the non-irradiated and irradiated at 16 dpa samples. The error is one standard deviation at 95% confidence interval. The imbalance from 100% is due to impurities (H, C, N, Si, Mn and Ga).

		Non-Irradiated (at%)	Irradiated (at%)
Total bulk concentration*	Cr	9.99 ± 0.04	9.7 ± 1.7
	Fe	87.50 ± 0.06	84.9 ± 2.5
	O	1.04 ± 0.04	2.2 ± 1.5
Matrix	Cr	10.24 ± 0.09	8.5 ± 0.3
	Fe	88.5 ± 0.3	89.1 ± 0.4
	O	0.15 ± 0.06	0.65 ± 0.18
Clusters**	Cr	9.0 ± 0.2	14.5 ± 1.2
	Fe	81.6 ± 0.8	60.5 ± 2.1
	O	6.4 ± 0.2	21.1 ± 1.2

* All the atoms measured within the APT tips.

** For the irradiated sample the mean value for the Cr and O-rich clusters (Fig. 5 and Fig. 7) are given, as separate accurate quantification is not possible.

we observe that the O and Cr content in the core of the cluster is around 37 at%. However, the dimensional extent of the Cr clustering is larger than that of the oxygen indicating a higher than O amount of Cr in the clusters. Further we may conclude that the number of Cr-O-rich clusters is the majority compared with the Cr-rich clusters observed in Fig. 5a and Fig. 7a.

4. Discussion

Fe-10at%Cr alloy films of 70 nm thickness were irradiated with 490 keV Fe⁺ ions at 300 °C to a damage dose of 20 dpa. PNR measurements show a reduction of Cr content in the matrix with the increase of dpa damage. After around four dpa the Cr concentration within the matrix has almost reached an equilibrium, i.e. after this dose and up to 20 dpa

no further changes are observed (Fig. 3 and Table 2). The fact that the system attains dynamic equilibrium after the dose of approximately four dpa is in alignment with the structural changes of the films as a function of the irradiation dose that were presented in our previous work [19]. In [19] it was observed that both the lattice constant and the crystallite size increase rapidly, as the irradiation dose increases, up to about the dose of four dpa and remain almost constant for further increase of the dose. Furthermore, the radiation damage kinetic constants for the crystallite size and the lattice constant, were found around 1.1 dpa and 2 dpa, respectively, in good agreement with the radiation damage kinetic constant for the solute Cr concentration (see Table 2), indicating similar behaviour with the accumulated irradiation dose.

The equilibrium concentration of Cr in the matrix found by the PNR measurements is 8.4 at% (Table 2). This is in excellent agreement with the value obtained by APT measurements (8.5 at%, Table 3). It has to be noted that the APT measurements were carried out in a sample irradiated with the dose of 16 dpa, i.e. being in the state of the dynamic equilibrium (see Fig. 3 and discussion above).

According to the modified Fe-Cr phase diagram proposed by Xiong et al. [16], Bonny et al. [41] and Zhao et al. [15] Fe-10at%Cr alloys are supersaturated alloys at the temperature of 300 °C. The matrix equilibrium of Cr at 300 °C suggested in [15] is around 8 at% which is very close to equilibrium concentration values of 8.4–8.5 at% (Table 2 and Table 3) derived from the PNR and APT measurements. Also the latter value is in agreement with the estimated solubility limit of Cr in Fe at 300 °C that has been reported in the literature. For example, Tissot et al. irradiated a high purity Fe-15at%Cr alloy with 1 MeV electrons up to 0.7 dpa and employing APT measurements estimated a solubility limit of (8.7 ± 0.5) at% which was reached after the dose of 0.2 dpa [42]. For neutron irradiated industrial purity Fe-12at%Cr alloys at the dose of 0.6 dpa the solubility limit has been estimated to be (8.5 ± 0.2) at% by Bergner et al. employing the SANS technique [43] and (8.24 ± 0.05) at% by Kuksenko et al. employing the APT technique [44].

Summarizing the above discussion at the equilibrium state, i.e. after four dpa irradiation, according to PNR and APT measurements around 1.6 at% of Cr has been removed from the matrix. This is, as discussed above, in accordance with the phase diagram which indicates that the formation of α' phase is thermodynamically favored (it should be noted that α' is the equilibrium phase to which Cr agglomerates will converge). The α' second phase formation at 300 °C is extremely slow during isothermal annealing [45] due to the slow diffusion of Cr in Fe. Second phase formation is strongly accelerated by irradiation, due to the supersaturation of point defects, leading to an acceleration of diffusion processes i.e. radiation-enhanced diffusion (RED) [46–48]. Our APT measurements show clustering of Cr atoms which is in accordance with the removal of Cr from the matrix observed from the PNR measurements. Before discussing these results a brief summary of the available information in the literature is undertaken.

Pintsuk et al. [49] proposed that the decomposition of alloys which contain oversized solute atoms (such as Fe-Cr alloys) under irradiation is driven by the internal strain that arises from the big difference in the relaxation volumes of Cr atoms in the Fe host material and of Fe atoms in the Cr host material. This difference is related to the different magnetic structure of these elements [50].

Indeed, α' precipitates have been experimentally observed to form in Fe-Cr alloys with Cr concentration greater than 9 at% that were irradiated at 300 °C with neutrons [43,44,47,51–55]. Contrary, in the case of self-ion irradiations at similar irradiation conditions, no α' precipitates with >85 at% Cr have been observed, but precipitates with modified characteristics compared to other forms of irradiation or thermal ageing have been identified. Specifically, Cr-rich clusters with a reduction in size, volume fraction and Cr content are observed [52,56–61]. Moreover, Cu⁺ ion irradiation at 475 °C of Fe-20 %Cr films was found to induce changes in their magnetic properties which were attributed to the formation of Cr-rich precipitates [62]. The difference in the morphology and content of the observed clusters in the case of ion

irradiation is mainly attributed to suppression mechanisms such as: the orders of magnitude higher damage rates compared to those in the case of neutrons, the high concentration of injected interstitials and ballistic dissolution.

APT measurements showed that oxygen is present in both samples and that it is also inhomogeneously distributed within the samples (see section 3.2). The contamination of the samples by oxygen cannot be pinpointed. As discussed in the experimental section sources as the starting sputtering target material, sputtering process, tip fabrication or oxygen atoms implantation during irradiations from the chromium oxide top layer have been excluded. Oxygen diffusion from the ambient after fabrication or during the long storage is a possibility which cannot be proved. Therefore, the subsequent discussion will incorporate both possibilities i.e. oxygen to be present before irradiations or to be incorporated after irradiations.

APT results show that in the non-irradiated sample Cr is homogeneously distributed i.e. there is no Cr clustering. In the non-irradiated sample only oxygen clusters with 6 at% oxygen, radius of gyration 6.8 nm and number density of 10^{23} m^{-3} are observed. In these clusters the Cr content within error is very close to that of that of the matrix (Table 3). Their volume fraction (calculated from the radius of gyration assuming spherical shapes) is around 28 % which corresponds to 1.8 at% oxygen concentration over the whole of the sample. This is a strong indication that most of the oxygen in the non-irradiated sample is contained within the observed oxygen clusters. This is consistent with the low solubility of oxygen in defect free Fe. Probably the term clustering is not appropriate as in reality oxygen-rich regions are observed (only 6 at% O compared with the homogeneous distribution of 10 at% of Cr) occupying a large fraction of the sample volume (28 %). The oxygen clustering also points to that there is stronger affinity between oxygen to oxygen than oxygen to Cr, i.e. towards the formation of oxygen-rich Cr phase (chromium oxide).

This clustering of oxygen needs to be explained. For agglomeration of oxygen initially diluted in the matrix we need to compare the mean distance of the agglomerates (around 30 nm) with the oxygen diffusion length ($R \sim \sqrt{Dt}$) (data for diffusion constant from [63]). The time needed for a diffusion length of 30 nm is 150 days. This is longer than the time elapsed between sample fabrication and ion irradiations (30 days). Thus, if we assume that the samples after fabrication contained diluted oxygen, we may infer that the oxygen clusters were not present during ion irradiations. On the contrary, as the time between fabrication and APT measurements were three years, oxygen agglomeration during sample storage can be explained. For oxygen diffusing at room temperature from the surface to the sample bulk for diffusion length of the total film thickness of 70 nm a time of 2.2 years is required. The time between sample fabrication and APT measurements has been about 3 years. Therefore after irradiation incorporation of oxygen is possible.

After Fe^+ ion irradiation at the dose of 16 dpa Cr accumulates into clusters having a radius of gyration of 2.4 nm and a number density of $6 \times 10^{23} \text{ m}^{-3}$. From these values, assuming spherical agglomerate, the volume fraction of agglomerates is 7.5 %. This volume fraction corresponds to 1.1 at% Cr and 1.6 at% O over the whole sample. The Cr content in the agglomerates found from PNR data i.e. ($c_o - c_{eq}$) (see Table 2) is (2.4 ± 0.4) at % and from APT data (subtraction from the total in the sample Cr to that found in the matrix, Table 3) is (1.2 ± 1.7) at %. These results indicate that the rough calculation of the volume fraction based on the radius of gyration gives reasonable values and support the consistency of the data from the experimental techniques. The oxygen concentration within the agglomerates (1.6 at%) is within errors equal to the total oxygen concentration in the sample (Table 3). This is a strong indication that most of the oxygen in the irradiated sample, as in the non-irradiated one, is contained within the observed clusters.

The important finding of the APT measurements is that the Cr removed from the matrix, as determined by PNR, agglomerates. Thus

the reduction of the Cr concentration in the matrix versus dpa damage in Fig. 3 can now be complemented by the observation that Cr agglomerates within the whole volume of the sample. The distribution of the Cr clusters as depicted in Fig. 5a and Fig. 7a does not suggest any correlation between their spacing and the size of the grain. Thus the nanocrystalline grain structure has not an observable effect on the Cr clustering.

Next the impact of oxygen on Cr clustering as a result of the irradiation will be discussed. As the morphology of oxygen in the sample to be irradiated (either not present, or diluted or in clusters) has not been established in a defensible form, all these possibilities will be considered.

If the oxygen is incorporated after irradiation, during the sample storage, the formation of oxygen clusters in the non-irradiated sample is compatible with the oxygen diffusivity at room temperature as discussed above. In the irradiated sample Cr clusters are formed by irradiation and the diffusing oxygen interacts with the Cr in the clusters forming $\text{CrO}_{1.5}$ (Table 3, 14.5 at% Cr and 21.1 at% O).

Another possibility is that the oxygen in the sample prior to the irradiations is randomly distributed in the matrix. If the oxygen was present in the as fabricated sample the time required for the observed agglomeration is larger than elapsed between fabrication and irradiations (see discussion above). Under irradiation enhanced diffusion takes place for both O and Cr species. As the oxygen energy for diffusion [63] is lower than that of Cr [64] oxygen agglomeration will occur faster than that of Cr. The formed oxygen clusters will then act as nucleation centres for the slower diffusing chromium. Heterogeneous nucleation is thermodynamically favourable as it lowers the surface free energy of the agglomerates. This form of agglomeration is suggested also from Fig. 8 in which it is apparent an oxygen rich core of the agglomerates.

Next will be assumed that the sample structure prior to the irradiation is that observed for the non-irradiated sample i.e. homogeneous distribution of Cr and most of the oxygen in oxygen rich areas of radius of gyration 6.8 nm, number density of 10^{23} m^{-3} and mean oxygen content 6 at%. After irradiation of 16 dpa again most of the oxygen is in Cr-O clusters having radius of gyration of 2.4 nm and a number density of $6 \times 10^{23} \text{ m}^{-3}$ and much higher than the non-irradiated sample oxygen content (around 21 at%). The after irradiation oxygen-rich clusters compared with those prior to the irradiation show a six fold increase of their number density, 25 times reduction of their volume and four fold increase of oxygen content. These results invalidate any assumption that the prior to irradiation oxygen clusters act as nucleation sites for the diffusing Cr. In reality, as it has been stressed above, in the non-irradiated state locally oxygen-rich areas are observed, not really clusters. What remains as explanation is that the O in the oxygen-rich areas (6 at%) diffusing under irradiation enhanced diffusivity forms clusters with core content around 35 at% (Fig. 8). These clusters act as nucleation centres for subsequent Cr agglomerations on them.

Summarizing the above, if oxygen is present prior to the irradiation, either in the form of oxygen rich areas or diluted in the matrix the same picture for Cr-O agglomerate formation emerges. The oxygen to a large extent forms clusters which subsequently act as nucleation sites for Cr agglomeration around them (see Fig. 8).

5. Summary and conclusions

490 keV Fe^+ ion irradiation of Fe-10at%Cr alloys in the form of thin films was carried out at the temperature of 300 °C, at the damage rate of 0.002 dpa/s and for doses ranging from 0.5 to 20 dpa. The Cr depletion from the Fe-Cr matrix, as deduced in our previous work [18,19] resulting from the self-ion irradiation of Fe-10at%Cr alloy films at 300 °C was further investigated employing APT measurements. The microstructural results of both the as-fabricated and the irradiated Fe-Cr alloy films have shown that the initially homogenous distribution of Cr in the Fe-Cr matrix changes after irradiation and Cr accumulates into clusters having up to 50 at% Cr and a mean Cr content of (14.5 ± 1.2) at

%, co-located with oxygen impurities. The clusters have a radius of gyration of (2.4 ± 1.4) nm and a number density of $6 \times 10^{23} \text{ m}^{-3}$. It is found that the system reaches a state of dynamic equilibrium after the dose of approximately 4 dpa. After this dose the solute Cr content presents a constant value of around (8.4 ± 0.3) at%, which is in agreement with the solubility limit of Cr in Fe that is reported in the literature for the irradiation temperature of 300 °C.

Moreover, the solute Cr concentration in the Fe-Cr matrix after irradiation at 16 dpa as determined by APT ($C_{Cr}^{APT}(16 \text{ dpa}) = (8.5 \pm 0.3)$ at%) agrees with that determined by PNR results ($C_{Cr}^{PNR}(16 \text{ dpa}) = (8.5 \pm 0.5)$ at%). In the latter case, the solute Cr concentration was determined from the magnetization of the films. The observed Cr depletion from the material's matrix is significant for the properties of the Fe-Cr alloy which depend on the solute Cr concentration. Nevertheless, further investigation of the results at radiation damage rates which are more relevant to a fusion reactor environment ($\sim 10^{-5}$ dpa/s) is needed. Considering that Cr clustering results in measurable changes in the magnetization [50] of the alloys, PNR can be used for the quantification of precipitation in Fe-Cr alloys up to depths up of about 500 nm. It is known that $\alpha - \alpha'$ decomposition of the Fe-Cr alloys can result in radiation-induced hardening and embrittlement [65]. Thus, magnetization measurements of the bulk or in film form materials can serve as a predictive non-destructive tool for their mechanical response.

Concerning the kinetics of Cr clustering the role of impurities and mainly of oxygen impurities needs to be elucidated and for that further investigations are necessary. In fusion or generally nuclear applications in which impure industrial materials will be used these issues are of paramount importance. Impurities do not only influence the diffusion process but also their agglomerates may act as nucleation sites.

CRedit authorship contribution statement

S. Pantousa: Writing – original draft, Formal analysis, Data curation. **A.J. London:** Writing – review & editing, Formal analysis, Data curation. **K. Mergia:** Writing – review & editing, Supervision, Resources, Project administration, Methodology, Investigation, Funding acquisition, Formal analysis, Conceptualization. **A. Ionescu:** Resources. **E. Manios:** Writing – review & editing, Data curation. **P. Tsavalas:** Data curation. **S. Dellis:** Data curation. **C. Kinane:** Resources, Data curation. **S. Langridge:** Writing – review & editing, Resources, Data curation. **A. Caruana:** Resources, Data curation. **U. Kentsch:** Resources. **S. Messoloras:** Writing – review & editing.

Declaration of competing interest

The authors declare that they have no known competing financial interests or personal relationships that could have appeared to influence the work reported in this paper.

Data availability

Data will be made available on request.

Acknowledgments

This work has been carried out within the framework of the EURO-fusion Consortium and has received funding from the Euratom research and training programme 2014-2018, 2019-2020 and 2021-2025 under Grant Agreements No. 633053 and No 101052200. The views and opinions expressed herein do not necessarily reflect those of the European Commission. Experiments at the ISIS Neutron and Muon Source were supported by a beamtime allocation from the Science and Technology Facilities Council [32,33]. The use of the Ion Beam Center facilities at Helmholtz-Zentrum Dresden-Rossendorf is acknowledged. The

research used UKAEA's Materials Research Facility, which has been funded by and is part of the UK's National Nuclear User Facility and Henry Royce Institute for Advanced Materials. Also, the funding from the Hellenic General Secretariat for Research and Innovation for the Greek National Programme for the Controlled Thermonuclear Fusion is acknowledged.

References

- [1] S.J. Zinkle, J.T. Busby, Structural materials for fission & fusion energy, Mater. Today. 12 (2009) 12–19, [https://doi.org/10.1016/S1369-7021\(09\)70294-9](https://doi.org/10.1016/S1369-7021(09)70294-9).
- [2] S.J. Zinkle, L.L. Snead, Designing Radiation Resistance in Materials for Fusion Energy, Doi: 10.1146/Annurev-Matsci-070813-113627. 44 (2014) 241–267. Doi: 10.1146/ANNUREV-MATSCI-070813-113627.
- [3] A.A.F. Tavassoli, E. Diegele, R. Lindau, N. Luzginova, H. Tanigawa, Current status and recent research achievements in ferritic/martensitic steels, J. Nucl. Mater. 455 (2014) 269–276, <https://doi.org/10.1016/j.jnucmat.2014.06.017>.
- [4] R. Lässer, N. Baluc, J.L. Boutard, E. Diegele, S. Dudarev, M. Gasparotto, A. Möslang, R. Pippan, B. Riccardi, B. van der Schaaf, Structural materials for DEMO: The EU development, strategy, testing and modelling, Fusion Eng. Des. 82 (2007) 511–520, <https://doi.org/10.1016/j.fusengdes.2007.06.031>.
- [5] P.M. Raole, S.P. Deshpande, Structural materials for fusion reactors, Trans. Indian Inst. Met. 62 (2009) 105–111, <https://doi.org/10.1007/s12666-009-0014-0>.
- [6] P. Arena, A. Del Nevo, F. Moro, S. Noce, R. Mozzillo, V. Imbriani, F. Giannetti, F. Edemetti, A. Froio, L. Savoldi, S. Siriano, A. Tassone, F. Roca Ugorri, P.A. Di Maio, I. Catanzaro, G. Bongiovì, The demo water-cooled lead–lithium breeding blanket: Design status at the end of the pre-conceptual design phase, Appl. Sci. 11 (2021), <https://doi.org/10.3390/AP112411592>.
- [7] G. Federici, W. Biel, M.R. Gilbert, R. Kemp, N. Taylor, R. Wenninger, European DEMO design strategy and consequences for materials, Nucl. Fusion. 57 (2017) 092002, <https://doi.org/10.1088/1741-4326/57/9/092002>.
- [8] F.A. Hernández, P. Pereslavtsev, G. Zhou, Q. Kang, S. D'Amico, H. Neuberger, L. V. Boccaccini, B. Kiss, G. Nádasi, L. Maqueda, I. Cristescu, I. Moscatu, I. Ricapito, F. Cisondi, Consolidated design of the HCPB Breeding Blanket for the pre-Conceptual Design Phase of the EU DEMO and harmonization with the ITER HCPB TBM program, Fusion Eng. Des. 157 (2020) 111614, <https://doi.org/10.1016/j.fusengdes.2020.111614>.
- [9] D. Terentyev, G. Bonny, N. Castin, Aspects of radiation damage effects in iron-chromium alloys from the point of view of atomistic modelling, in: Int. Conf. Nucl. Eng. Proceedings, ICONE, 2009: pp. 899–907. Doi: 10.1115/ICONE17-75636.
- [10] F.A. Garner, M.B. Toloczko, B.H. Sencer, Comparison of swelling and irradiation creep behavior of fcc-austenitic and bcc-ferritic/martensitic alloys at high neutron exposure, JNuM. 276 (2000) 123–142, [https://doi.org/10.1016/S0022-3115\(99\)00225-1](https://doi.org/10.1016/S0022-3115(99)00225-1).
- [11] R.L. Klueh, D.R. Harries, ASTM International., High-chromium ferritic and martensitic steels for nuclear applications, (2001) 221.
- [12] P. Yvon, F. Carré, Structural materials challenges for advanced reactor systems, J. Nucl. Mater. 385 (2009) 217–222, <https://doi.org/10.1016/j.jnucmat.2008.11.026>.
- [13] M.B. Toloczko, F.A. Garner, C.R. Eiholzer, Irradiation creep and swelling of the US fusion heats of HT9 and 9Cr-1Mo to 208 dpa at $\sim 400^\circ\text{C}$, J. Nucl. Mater. 212–215 (1994) 604–607, [https://doi.org/10.1016/0022-3115\(94\)90131-7](https://doi.org/10.1016/0022-3115(94)90131-7).
- [14] G. Bonny, D. Terentyev, L. Malerba, New Contribution to the Thermodynamics of Fe-Cr Alloys as Base for Ferritic Steels, (n.d.). Doi: 10.1007/s11669-010-9782-9.
- [15] Y. Zhao, Y. Li, A. Bhattacharya, J.D. Poplawsky, J. Henry, S. Zinkle, Determining the Phase Boundary between α and α' in Fe-Cr Alloys with Proton Irradiations and Thermal Aging, (n.d.). Doi: 10.2139/SSRN.4434695.
- [16] W. Xiong, M. Selleby, Q. Chen, J. Odqvist, Y. Du, Phase equilibria and thermodynamic properties in the Fe-Cr system, Crit. Rev. Solid State Mater. Sci. 35 (2010) 125–152, <https://doi.org/10.1080/10408431003788472>.
- [17] I.A.E. AGENCY, Fundamentals of Magnetic Fusion Technology, Fundam. Magn. Fusion Technol. (2023) 1–750. <https://www.iaea.org/publications/14898/fundamentals-of-magnetic-fusion-technology> (accessed October 3, 2023).
- [18] K. Mergia, E.O. Tsompopoulou, S. Dellis, C.H. Marrows, I. Michelakaki, C. Kinane, A. Caruana, S. Langridge, A.P. Douvalis, C. Cabet, S. Messoloras, Phase stability of Fe-5at%Cr and Fe-10at%Cr films under Fe+ ion irradiation, J. Phys. Condens. Matter. 32 (2020), <https://doi.org/10.1088/1361-648X/ab69a1>.
- [19] S. Pantousa, K. Mergia, A. Ionescu, E. Manios, S. Dellis, C. Kinane, S. Langridge, A. Caruana, U. Kentsch, S. Messoloras, Fe+ ion irradiation effects in Fe-10at%Cr films irradiated at 300 °C, Nucl. Mater. Energy. 30 (2022) 101147, <https://doi.org/10.1016/j.nme.2022.101147>.
- [20] K. Papamihail, K. Mergia, F. Ott, Y. Serruys, T. Speliotis, G. Apostolopoulos, S. Messoloras, Fe+ ion irradiation induced changes in structural and magnetic properties of iron films, Nucl. Mater. Energy. 9 (2016) 459–464, <https://doi.org/10.1016/j.nme.2016.03.006>.
- [21] K. Papamihail, K. Mergia, F. Ott, Y. Serruys, T. Speliotis, G. Apostolopoulos, S. Messoloras, Magnetic effects induced by self-ion irradiation of Fe films, Phys. Rev. B. 93 (2016), <https://doi.org/10.1103/PhysRevB.93.100404>.
- [22] R.S. Nelson, Contemporary Physics The use of ion beams to study radiation effects in metals The Use of Ion Beams to Study Radiation Effects in Metals, 19 (1978) 543–560. Doi: 10.1080/00107517808207700.
- [23] S.J. Zinkle, L.L. Snead, Opportunities and limitations for ion beams in radiation effects studies: Bridging critical gaps between charged particle and neutron

- irradiations, *Scr. Mater.* 143 (2018) 154–160, <https://doi.org/10.1016/J.SCRIPMAT.2017.06.041>.
- [24] J.F. Ziegler, M.D. Ziegler, J.P. Biersack, SRIM – The stopping and range of ions in matter (2010), *Nucl. Instruments Methods Phys. Res. Sect. B Beam Interact. with Mater. Atoms.* 268 (2010) 1818–1823. Doi: 10.1016/J.NIMB.2010.02.091.
- [25] James Ziegler - SRIM & TRIM, (n.d.). <http://www.srim.org/> (accessed October 27, 2021).
- [26] ASTM, E521-96: Standard Practice for Neutron Radiation Damage Simulation by Charged-Particle, *Annu. B. ASTM Stand.* 12.02 (2009) 1–21. Doi: 10.1520/E0521-96R09E02.
- [27] K. Nordlund, S.J. Zinkle, A.E. Sand, F. Granberg, R.S. Averback, R. Stoller, T. Suzudo, L. Malerba, F. Banhart, W.J. Weber, F. Willaime, S.L. Dudarev, D. Simeone, Improving atomic displacement and replacement calculations with physically realistic damage models, *Nat. Commun.* 9 (2018), <https://doi.org/10.1038/s41467-018-03415-5>.
- [28] S. Agarwal, Y. Lin, C. Li, R.E. Stoller, S.J. Zinkle, On the use of SRIM for calculating vacancy production: Quick calculation and full-cascade options, *Nucl. Instruments Methods Phys. Res. Sect. B Beam Interact. Mater. Atoms.* 503 (2021) 11–29, <https://doi.org/10.1016/J.NIMB.2021.06.018>.
- [29] Y. Sun, S.Z. Diao, P.P. Liu, Q. Zhan, F.R. Wan, Anomalies in the calculation of dpa by using damage energy method based on full-cascades option of SRIM, *Ann. Nucl. Energy.* 183 (2023) 109667, <https://doi.org/10.1016/J.ANUCENE.2022.109667>.
- [30] R.E. Stoller, M.B. Toloczko, G.S. Was, A.G. Certain, S. Dwaraknath, F.A. Garner, On the use of SRIM for computing radiation damage exposure, *Nucl. Instruments Methods Phys. Res. Sect. B Beam Interact. Mater. Atoms.* 310 (2013) 75–80, <https://doi.org/10.1016/J.NIMB.2013.05.008>.
- [31] J.F. Ankner, G.P. Felcher, Polarized-neutron reflectometry, *J. Magn. Magn. Mater.* 200 (1999) 741–754, [https://doi.org/10.1016/S0304-8853\(99\)00392-3](https://doi.org/10.1016/S0304-8853(99)00392-3).
- [32] K. Mergia, S. Messoloras, S. Dellis, I. Michelakaki, S. Langridge, C. Kinane, E. Manios, S. Pantousa, Polarised Neutron Reflectivity investigation of Fe+ ion irradiated Fe-20at%Cr film alloys, 2019. Doi: 10.5286/ISIS.E.RB1910183.
- [33] K. Mergia, C. Kinane, E. Manios, S. Langridge, S. Dellis, S. Pantousa, S. Messoloras, Effect of the irradiation temperature on the magnetic state of Fe+ ion irradiated FeCr films, 2020. <https://doi.org/Doi:10.5286/ISIS.E.RB2010432>.
- [34] Welcome to GenX's documentation! — GenX 3.6.21 documentation, (n.d.). <https://aglavic.github.io/genx/doc/> (accessed April 19, 2023).
- [35] A. Glavic, M. Björck, GenX 3: the latest generation of an established tool, *J. Appl. Cryst.* 55 (2022) 1063–1071, <https://doi.org/10.1107/S1600576722000653>.
- [36] M.K. Miller, K.F. Russell, K. Thompson, R. Alvis, D.J. Larson, Review of atom probe FIB-based specimen preparation methods, *Microsc. Microanal.* 13 (2007) 428–436, <https://doi.org/10.1017/S1431927607070845>.
- [37] M.K. Miller, R.G. Forbes, Introduction to atom-probe tomography, *Atom-Probe Tomogr.* (2014) 1–49, https://doi.org/10.1007/978-1-4899-7430-3_1.
- [38] D. Blavette, B. Deconihout, A. Bostel, J.M. Sarrau, M. Bouet, A. Menand, The tomographic atom probe: A quantitative three-dimensional nanoanalytical instrument on an atomic scale, *Rev. Sci. Instrum.* 64 (1993) 2911–2919, <https://doi.org/10.1063/1.1144382>.
- [39] E.A. Jägle, P.P. Choi, D. Raabe, The maximum separation cluster analysis algorithm for atom-probe tomography: Parameter determination and accuracy, *Microsc. Microanal.* 20 (2014) 1662–1671, <https://doi.org/10.1017/S1431927614013294>.
- [40] A.J. London, Quantifying uncertainty from mass-peak overlaps in atom probe microscopy, *Microsc. Microanal.* 25 (2019) 378–388, <https://doi.org/10.1017/S1431927618016276>.
- [41] G. Bonny, D. Terentyev, L. Malerba, On the α - α' miscibility gap of Fe-Cr alloys, *Scr. Mater.* 59 (2008) 1193–1196, <https://doi.org/10.1016/j.scriptamat.2008.08.008>.
- [42] O. Tissot, C. Pareige, E. Meslin, B. Decamps, J. Henry, Kinetics of α' precipitation in an electron-irradiated Fe15Cr alloy, *Scr. Mater.* 122 (2016) 31–35, <https://doi.org/10.1016/j.scriptamat.2016.05.021>.
- [43] F. Bergner, A. Ulbricht, C. Heintze, Estimation of the solubility limit of Cr in Fe at 300 °C from small-angle neutron scattering in neutron-irradiated Fe-Cr alloys, *Scr. Mater.* 61 (2009) 1060–1063, <https://doi.org/10.1016/j.scriptamat.2009.08.028>.
- [44] V. Kuksenko, C. Pareige, P. Pareige, Intra granular precipitation and grain boundary segregation under neutron irradiation in a low purity Fe-Cr based alloy, in: *J. Nucl. Mater., North-Holland* (2012) 125–129, <https://doi.org/10.1016/j.jnucmat.2011.10.031>.
- [45] P.J. Grobner, The 885° f (475° c) embrittlement of ferritic stainless steels, *Metall. Trans.* 4 (1973) 251–260, <https://doi.org/10.1007/BF02649625>.
- [46] F. Soisson, T. Jourdan, Radiation-accelerated precipitation in Fe-Cr alloys, *Acta Mater.* 103 (2015) 870–881, <https://doi.org/10.1016/j.actamat.2015.11.001>.
- [47] M. Bachhav, G. Robert Odette, E.A. Marquis, α' precipitation in neutron-irradiated Fe-Cr alloys, *Scr. Mater.* 74 (2014) 48–51, <https://doi.org/10.1016/j.scriptamat.2013.10.001>.
- [48] M.H. Mathon, Y. De Carlan, G. Geoffroy, X. Averty, A. Alamo, C.H. De Novion, A SANS investigation of the irradiation-enhanced α - α' phases separation in 7–12 Cr martensitic steels, *J. Nucl. Mater.* 312 (2003) 236–248, [https://doi.org/10.1016/S0022-3115\(02\)01630-6](https://doi.org/10.1016/S0022-3115(02)01630-6).
- [49] G. Pintsuk, G. Aiello, S.L. Dudarev, M. Gorley, J. Henry, M. Richou, M. Rieth, D. Terentyev, R. Vila, Materials for in-vessel components, *Fusion Eng. Des.* 174 (2022) 112994, <https://doi.org/10.1016/J.FUSENGDES.2021.112994>.
- [50] J.B.J. Chapman, P.W. Ma, S.L. Dudarev, Dynamics of magnetism in Fe-Cr alloys with Cr clustering, *Phys. Rev. B.* 99 (2019) 184413, <https://doi.org/10.1103/PhysRevB.99.184413>.
- [51] W.Y. Chen, Y. Miao, Y. Wu, C.A. Tomchik, K. Mo, J. Gan, M.A. Okuniewski, S. A. Maloy, J.F. Stubbins, Atom probe study of irradiation-enhanced α precipitation in neutron-irradiated Fe-Cr model alloys, *J. Nucl. Mater.* 462 (2015) 242–249, <https://doi.org/10.1016/j.jnucmat.2015.04.005>.
- [52] C. Pareige, V. Kuksenko, P. Pareige, Behaviour of P, Si, Ni impurities and Cr in self ion irradiated Fe-Cr alloys - Comparison to neutron irradiation, *J. Nucl. Mater.* 456 (2015) 471–476, <https://doi.org/10.1016/j.jnucmat.2014.10.024>.
- [53] E.R. Reese, M. Bachhav, P. Wells, T. Yamamoto, G. Robert Odette, E.A. Marquis, On α' precipitate composition in thermally annealed and neutron-irradiated Fe-9–18Cr alloys, *J. Nucl. Mater.* 500 (2018) 192–198, <https://doi.org/10.1016/j.jnucmat.2017.12.036>.
- [54] M. Hernández-Mayoral, C. Heintze, E. Oñorbe, Transmission electron microscopy investigation of the microstructure of Fe-Cr alloys induced by neutron and ion irradiation at 300°C, *J. Nucl. Mater.* 474 (2016) 88–98, <https://doi.org/10.1016/j.jnucmat.2016.03.002>.
- [55] V. Kuksenko, C. Pareige, P. Pareige, Cr precipitation in neutron irradiated industrial purity Fe–Cr model alloys, *J. Nucl. Mater.* 432 (2013) 160–165, <https://doi.org/10.1016/J.JNUCMAT.2012.07.021>.
- [56] E.R. Reese, N. Almirall, T. Yamamoto, S. Tumey, G. Robert Odette, E.A. Marquis, Dose rate dependence of Cr precipitation in an ion-irradiated Fe[bn]d18Cr alloy, *Scr. Mater.* 146 (2018) 213–217, <https://doi.org/10.1016/j.scriptamat.2017.11.040>.
- [57] E. Marquis, B. Wirth, G. Was, Characterization and Modeling of Grain Boundary Chemistry Evolution in Ferritic Steels under Irradiation, (2016). Doi: 10.2172/1248953.
- [58] O. Tissot, C. Pareige, E. Meslin, B. Décamps, J. Henry, Influence of injected interstitials on α' precipitation in Fe-Cr alloys under self-ion irradiation, (2016). Doi: 10.1080/21663831.2016.1230896.
- [59] K.N. Thomas, G.S. Was, Effect of cascade size and damage rate on α' precipitate stability in Fe-15Cr, *J. Nucl. Mater.* 585 (2023) 154615, <https://doi.org/10.1016/J.JNUCMAT.2023.154615>.
- [60] Y. Zhao, A. Bhattacharya, C. Pareige, C. Massey, P. Zhu, J.D. Poplawsky, J. Henry, S.J. Zinkle, Effect of heavy ion irradiation dose rate and temperature on α' precipitation in high purity Fe-18%Cr alloy, *Acta Mater.* 231 (2022) 117888, <https://doi.org/10.1016/J.ACTAMAT.2022.117888>.
- [61] C.D. Hardie, S.G. Roberts, Nanoindentation of model Fe-Cr alloys with self-ion irradiation, *J. Nucl. Mater.* 433 (2013) 174–179, <https://doi.org/10.1016/j.jnucmat.2012.09.003>.
- [62] Y. Kamada, H. Watanabe, S. Mitani, J.N. Mohapatra, H. Kikuchi, S. Kobayashi, M. Mizuguchi, K. Takanashi, Ion-irradiation enhancement of materials degradation in Fe–Cr single crystals detected by magnetic technique, *J. Nucl. Mater.* 442 (2013) S861–S864, <https://doi.org/10.1016/J.JNUCMAT.2012.11.042>.
- [63] J. Takada, M. Adachi, Determination of diffusion coefficient of oxygen in α -iron from internal oxidation measurements in Fe-Si alloys, *J. Mater. Sci.* 21 (1986) 2133–2137, <https://doi.org/10.1007/BF00547959/METRICS>.
- [64] C.-G. Lee, Y. Iijima, T. Hiratani, K. Hirano, Diffusion of Chromium in α -Iron, *Mater. Trans. JIM.* 31 (1990) 255–261, <https://doi.org/10.2320/matertrans1989.31.255>.
- [65] C.D. Hardie, C.A. Williams, S. Xu, S.G. Roberts, Effects of irradiation temperature and dose rate on the mechanical properties of self-ion implanted Fe and Fe-Cr alloys, *J. Nucl. Mater.* 439 (2013) 33–40, <https://doi.org/10.1016/j.jnucmat.2013.03.052>.